Triglobal Shock Buffet Instability Study on Infinite Wings

Wei He* and Sebastian Timme[†]

University of Liverpool, Liverpool, L69 3GH, United Kingdom

Triglobal stability analysis is presented to address the question of shock-buffet unsteadiness and dominant modal behaviour on infinite wings at high Reynolds number. This contribution expands upon recent biglobal work by Crouch et al. [1], Paladini et al. [2] and Plante et al. [3] aspiring to elucidate the origin and characteristics of shock buffet on finite swept wings. Our infinite wings are modelled by extruding an OAT15A aerofoil with different physical aspect ratios and imposing a spanwise translational periodic boundary condition without assumptions on spanwise homogeneity. The flow is described by the Reynolds-averaged Navier–Stokes equations with closure via Spalart–Allmaras turbulence modelling. Flow conditions are a Mach number of 0.73, a chord Reynolds number of 3.2×10^6 and different angles of attack around instability onset. The critical angle of attack is approximately 3.4°, similar to previous aerofoil results in Sartor et al. [4]. Two distinct steady base flows, spanwise parallel and non-parallel, are analysed herein on straight and swept wings. Triglobal stability analysis of the spanwise parallel flow on the infinite-straight wing with aspect ratio three identifies both an unstable oscillatory mode, linked to the spanwise-uniform chordwise shock motion synchronised with a pulsation of its downstream shear layer, and several monotone (non-oscillatory) spanwise-periodic shock-distortion modes. Those monotone modes become oscillatory and outboard travelling on the swept wings with their frequencies and phase speeds correlated to the sweep angle. In non-parallel flow on straight wings of different aspect ratios, two dominant three-dimensional modes are found, both stable and unstable depending on aspect ratio. Non-linear time-marching simulations confirm the insights gained from linear stability analysis.

Nomenclature

$\mathcal{AR}$	=	aspect ratio $\equiv$ b/c
b	=	wing span
C_D	=	drag coefficient
C_L	=	lift coefficient
C_p	=	pressure coefficient
c	=	chord
L	=	wavelength of spanwise-periodic mode
l	=	length between two foci in each buffet cell
M	=	Mach number
n_y	=	number of points in spanwise direction
Re	=	Reynolds number
R_ρ	=	density residual
St	=	Strouhal number
$U_{\infty,n}$	=	reference velocity in plane perpendicular to the leading edge
U_∞	=	freestream velocity
α	=	angle of attack (°)
β	=	spanwise wavenumber, $\beta \equiv 2\pi/L$
λ	=	eigenvalue ($= \sigma + i\omega$) with σ as growth/decay rate and ω as angular frequency
Δy	=	grid spacing in spanwise direction
Λ	=	sweep angle (°)

---

*Research Associate, School of Engineering, wei.he@liverpool.ac.uk. Member AIAA.

[†]Senior Lecturer, School of Engineering, sebastian.timme@liverpool.ac.uk. Member AIAA.

I. Introduction

Sʜᴏᴄᴋ buffet brings a challenge to the wing design of modern large transport-type aircraft when flying in the transonic regime. Shock buffet will exert additional low-frequency aerodynamic loads on the wing affecting the flight performance and potentially causing damage to the structure. Jacquin et al. [5] documented a stable shock in the transonic flow ($M = 0.73$, $Re \approx 3 \times 10^6$) of a low aspect ratio (approximately $\mathit{Æ} = 3.4$) wing at angles of attack $\alpha \lessapprox 3°$. With increasing angle of attack, the shock becomes unstable leading to a strong oscillation of the shock-wave/turbulent boundary-layer separation, referred to as 'shock buffet', at approximately $\alpha = 3.5°$. After the onset of shock buffet, a three-dimensional flow pattern is formed in the separation zone behind the unsteady shock. It resembles the so-called 'stall cells' observed in the flow of severe separation from low to high Reynolds numbers [3, 6–11]. Numerical simulations on different aerofoils at high Reynolds numbers featuring shock oscillations showed that the flow can be approximated through solving the unsteady Reynolds-averaged Navier–Stokes (RANS) equations together with an appropriate turbulence model [12–14], hence relying on the assumption of a separation of scales between the large-scale low-frequency coherent shock-buffet dynamics, accessible through the unsteady RANS method, and the small spatial and temporal scales of turbulence. The prediction of shock-buffet onset is nevertheless expensive regardless if flight test, wind tunnel test or time-stepping unsteady simulations is used, and modal stability methods based on the linearised governing equations are an attractive alternative [1, 4, 15].

Stability analysis was first shown to be an effective method in predicting the onset of two-dimensional aerofoil shock buffet by Crouch et al. [15]. Those transonic-flow stability results on a NACA0012 aerofoil demonstrated good agreement with earlier experimental data [16]. More recently, the ideas were successfully applied in the analysis of other aerofoils [4, 17] and three-dimensional infinite and finite wings [1–3, 18–20]. In those infinite-wing shock-buffet stability studies, the authors either predicted the spanwise-periodic modes in the framework of biglobal stability analysis [1] or solved the fully three-dimensional stability problem on small aspect ratio wings albeit using symmetric (instead of periodic) boundary condition [17]. Through carrying out triglobal stability analysis, Iorio et al. [17] suggested that a two-dimensional study is sufficient to predict the buffet onset. However, a spanwise-periodic stationary monotone mode can be most amplified for certain wing geometries and flow conditions, as demonstrated in recent work by Crouch et al. [1], Paladini et al. [2] and Plante et al. [3]. Discrepancies in predictions could result from using different wings of small aspect ratio, typically $\mathit{Æ} \leqslant 4$, or from imposing either spanwise symmetric or periodic boundary conditions. Triglobal stability analysis on the infinite wing, both straight and swept, is currently missing to link shock-buffet characteristics on the infinite wing, derived from biglobal studies, with those on the finite wing [19–21].

Once the shock-buffet phenomenon appears, three-dimensional separation cells are formed on the suction side of the wing. Biglobal stability analysis on a two-dimensional base flow in the absence of a spanwise flow field variation is not sufficient to describe the complete picture of perturbation modes. Triglobal stability analysis can deal with an arbitrary three-dimensional flow field on a complex geometry, without an assumption on homogeneity in any spatial dimension, i.e. irrespective of assuming a homogeneous flow field in the spanwise direction as done in biglobal studies. In this paper, we are interested in understanding the fully three-dimensional perturbation dynamics, without simplifying assumptions, by describing the isolated impact of key geometric wing-sizing parameters (such as aspect ratio and sweep) and flow conditions (such as angle of attack) in the formation and characteristics of the shock-buffet instability near onset. The infinite straight and swept wings herein are modelled using different actual aspect ratios while imposing a spanwise periodic boundary condition, as described in Sec. II. In Sec. III, the development of the three-dimensional base flow with respect to a varying angle of attack and sweep angle around the OAT15A profile is presented. Flow conditions (normal to leading edge) are a chord Reynolds number of 3.2×10^6 and a freestream Mach number of 0.73, which agree with previous studies on the same geometry [1, 4, 5]. Then, in Sec. IV, triglobal linear stability analysis is discussed for parallel base flow on the straight and swept wing as well as non-parallel flow on the straight wing.

II. Numerical Setup

A. Infinite Wing Definition

Infinite straight wings are defined by extruding a two-dimensional OAT15A aerofoil mesh (see fig. 1) in spanwise direction to have aspect ratios between one and ten, and using an appropriate spanwise periodic boundary condition as outlined below. This aerofoil is the same profile used by Jacquin et al. [5] in the experiments and by Sartor et al. [4] and Crouch et al. [1] in their respective stability analyses. The two-dimensional baseline domain is circular with a radius of 100 chord lengths, which is discretised by approximately 35 000 points. Viscous walls impose a no-slip boundary condition, the outer boundary is described as farfield, and a translational periodic boundary condition is
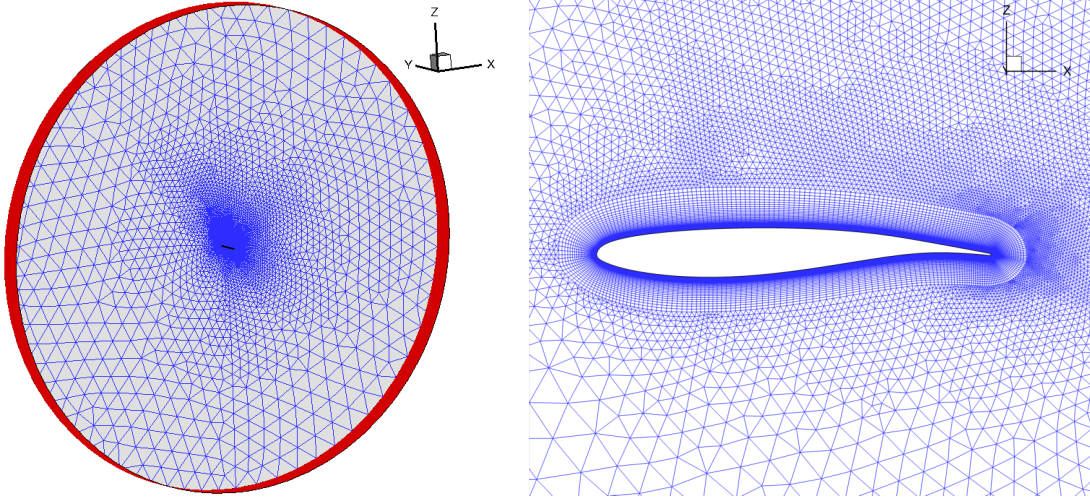
Fig. 1   Overall perspective of three-dimensional grid (left) and zoomed view around the aerofoil (right).
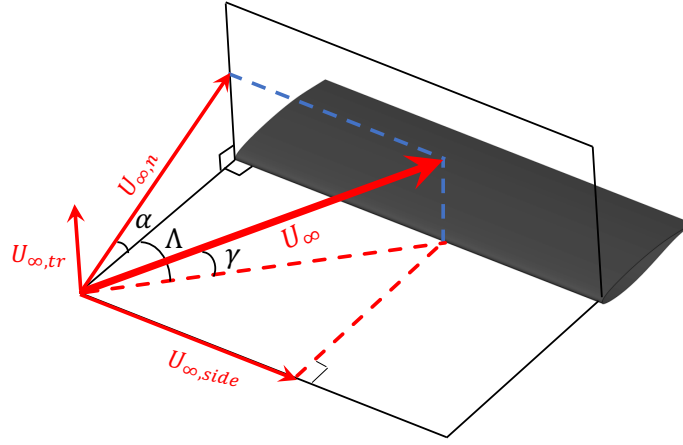

Fig. 2   Swept wing flow setup.

defined at either end of the span. The boundary-layer region is structured ensuring $y^+ < 1$, while an unstructured mesh is chosen elsewhere towards the farfield boundary. In the baseline extruded mesh for the infinite wing, there are 20 points uniformly distributed per unit length in span, while a more detailed spanwise grid convergence study can be found in the Appendix.

Swept wings are an integral part in designing modern transport aircraft, on account of a better high speed aerodynamic performance. Figure 2 shows the definition of the flow past a wing with a non-zero sweep angle Λ. Parameters α, $U_{\infty,n}$ and $Re_{\infty,n}$ are the components of angle of attack, reference velocity and Reynolds number perpendicular to the leading edge of the wing, respectively. Herein the infinite swept-wing flow is modelled by adjusting the direction and magnitude of the freestream velocity vector, instead of modifying the wing shape or orientation, to ensure constant flow conditions in the plane normal to the leading edge, by using the transformations

$$
\begin{aligned}
U_\infty &= \frac{U_{\infty,n}}{\cos\Lambda} \sqrt{1 - \sin^2\alpha \, \sin^2\Lambda}, \\
Re_\infty &= \frac{Re_{\infty,n}}{\cos\Lambda} \sqrt{1 - \sin^2\alpha \, \sin^2\Lambda}, \\
\gamma &= \mathrm{atan}(\tan\alpha \, \cos\Lambda).
\end{aligned}
\tag{1}
$$

As reference length, we use consistently the chord length of the aerofoil normal to the leading edge.

Table 1 **Steady-state lift and drag coefficients at different angles of attack for $\mathcal{R} = 3$ wing.**

α (°)	$\bar{C}_L$	$\bar{C}_D$
3.2	0.976938	0.040644
3.3	0.978152	0.042304
3.4	0.912120	0.042416
3.5	0.910152	0.043981

B. Numerical Methods

Both the steady and unsteady RANS equations are solved using the DLR–TAU solver, which is a second-order finite-volume code capable of dealing with complex geometries [22]. For modelling the Reynolds stresses we make use of the negative version of the Spalart-Allmaras (S-A) turbulence model [23]. The inviscid fluxes of the mean flow equations are discretised using a central scheme with matrix artificial dissipation, whereas a first-order Roe scheme is used for those of the turbulence model. Gradients of flow variables are computed using the Green–Gauss approach. As time-stepper, we chose an explicit Runge–Kutta scheme with local time-stepping and geometric multigrid (normally on three grid levels) for convergence acceleration. For unsteady time-marching simulations, the second-order backward difference formula is adopted. Cauchy convergence control on the drag coefficient is chosen with a minimum of 50 iterations in dual time per real time step, and a time-step size is defined to have about 1000 to 2000 physical time steps per period of a shock-buffet oscillation.

A triglobal stability tool, using implicitly restarted Arnoldi method with shift-and-invert spectral transformation and sparse iterative linear equation solver, has been implemented into the TAU code previously and its ability was demonstrated in [18–20]. The numerical approach follows a first-discretise-then-linearise matrix-forming philosophy, with a hand-differentiated Jacobian matrix, using an iterative inner-outer solution scheme. The steady-state RANS solution (fully coupled with the turbulence model) is used as base flow, denoted $\bar{u}$ and containing the conservative variables of density, three momentum components, total energy and the turbulence variable, around which the linearised system is formed, leading to the eigenvalue problem

$$J\hat{u} = \lambda\hat{u} \qquad (2)$$

where J is the discrete flux Jacobian matrix corresponding to the chosen spatial discretisation including all boundary conditions, and $\hat{u}$ and λ are eigenvector and eigenvalue, respectively. The eigenvalue $\lambda = \sigma + i\omega$ describes exponential growth or decay (σ) and frequency of an oscillation (ω). The eigenvector contains the complex-valued spatial amplitudes of the linear perturbation around the base flow, $\tilde{u} = \hat{u}e^{\lambda t}$, where $\varepsilon\tilde{u} = u - \bar{u}$ and t is time. The Arnoldi method [24], as implemented in the ARPACK library [25, 26], is used to approximate a few but relevant eigenmodes in the outer iteration. A preconditioned sparse iterative Krylov subspace solver [27] is applied for the solution of the inner linear systems arising from the shift-and-invert strategy, where Arnoldi's method is applied to $(J - \zeta I)^{-1}$ (instead of J) with ζ as arbitrary shift. The established numerical strategy combined with an industrial computational fluid dynamics solver means that even practical non-canonical test cases at high Reynolds number flow condition can be investigated.

Dealing with the linearised translational periodic boundary condition in this work is a delicate matter. Since a complete analytical hand-differentiated Jacobian matrix of this boundary condition is currently not available in the code, we made use of the analytical formulation where possible (i.e. internal points) and implemented a numerical central finite-difference approach using graph colouring where necessary. Care has to be taken that shadow periodic points are discarded in the Jacobian matrix altogether and any dependence on those points is transferred to the location of the corresponding master periodic points.

III. Base Flow Classification

In an earlier experimental study [5], the flow is steady for a small aspect ratio $\mathcal{R} \approx 3.4$ below an angle of attack $\alpha \lessapprox 3.0°$ at freestream Mach number of $M = 0.73$ and an approximate Reynolds number of 3.2×10^6. Surface oil flow visualization showed that the surface lines on the suction side of this wing are essentially two-dimensional parallel. With increase in angle of attack, shock oscillation was found as well as a three-dimensional separation behind the shock. These phenomena can be examined using an appropriate RANS simulation. Using the same values of Mach number and Reynolds number, as stated above for the experimental conditions, for the straight wing flow, the surface
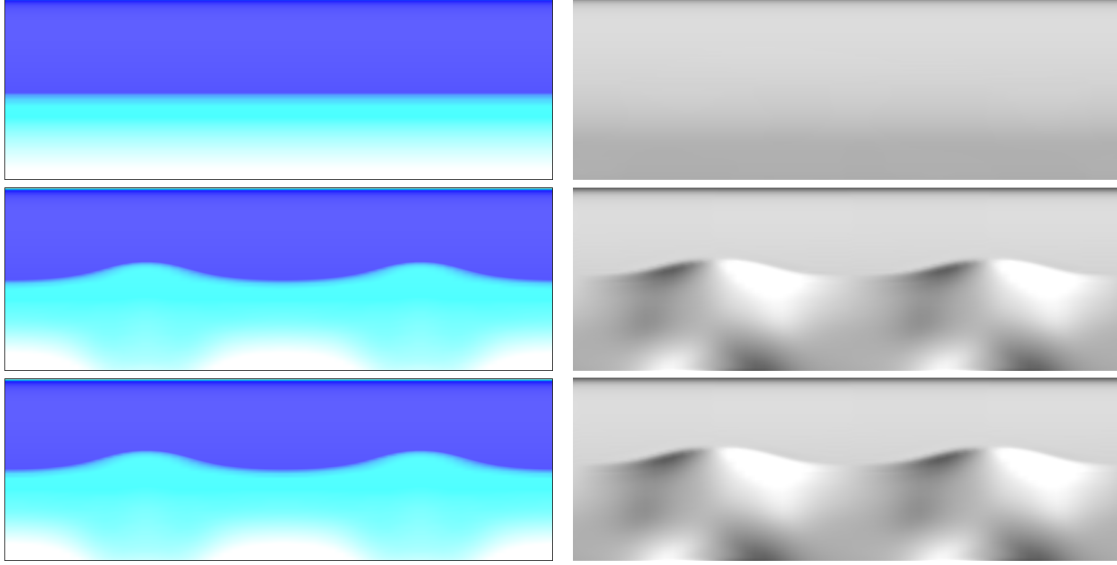
Fig. 3 Surface pressure coefficient $\bar{C}_p$ (left column) and spanwise skin-friction component $\bar{C}_{f_y}$ (right column) on the upper wing surface as a function of angle of attack for a $A\!R = 3$ wing with $n_y = 60$ points along the span. Angles of attack from top to bottom are $\alpha = 3.3°$, $3.4°$ and $3.5°$. Contour levels of $\bar{C}_p$ are in range $[-1, 1]$ and of $\bar{C}_{f_y}$ in range $[-10^{-6}, 10^{-6}]$. Flow direction is from top to bottom.
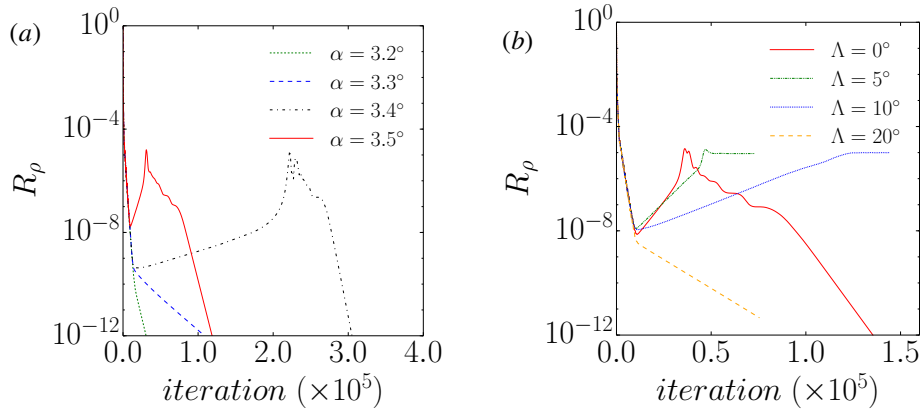

Fig. 4 Convergence history of density residual norm R_ρ for $A\!R = 3$ wing showing (a) different angles of attack for straight wing and (b) different sweep angles at $\alpha = 3.5°$.

flow field corresponding to the well converged RANS simulation at angles of attack around the onset of shock buffet is presented in fig. 3. The figure reveals the three-dimensional cellular pattern at higher angles of attack, which can also be related to the nonlinear trend in the convergence history in fig. 4(a), outlined in the next paragraph. Besides the surface pressure coefficient shown in fig. 3 (left column), we examined another variable, specifically the spanwise skin-friction component C_{f_y} (see fig. 3 (right column)), giving the same conclusion. The corresponding lift and drag coefficients (C_L and C_D) are listed in table 1. It can be seen that C_L increases with increasing α, reaching its maximum just before the formation of the cellular pattern. The drag coefficient on the other hand keeps increasing with angle of attack regardless.

Although steady-state RANS results are time-independent, useful insight can be extracted by analysing the residual history to estimate the expected flow unsteadiness. Figure 4(a) shows the complete convergence behaviour of the density residual norm (labelled R_ρ) of the steady RANS equations from low to high angles of attack on the straight wing. Two types of nominally steady flow characteristics, specifically parallel and non-parallel flow, can be identified depending on the state of convergence of residual R_ρ. This is discussed in the following for both straight and swept wings.
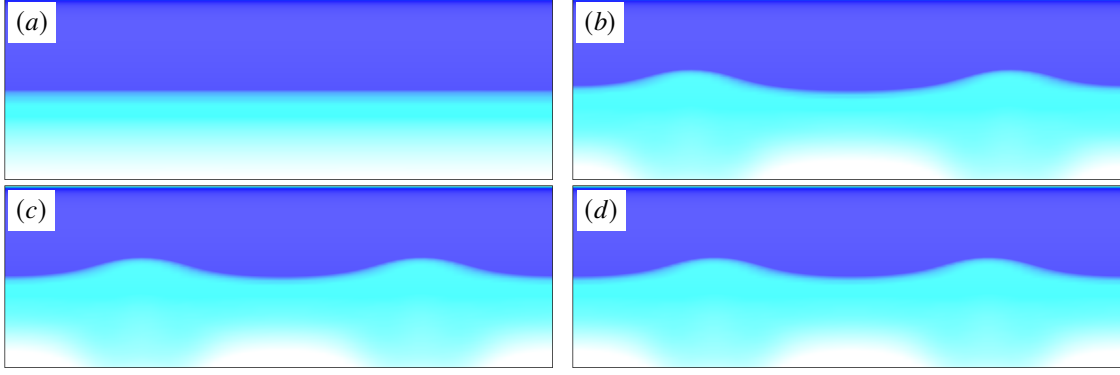
5

Fig. 5 Evolution of surface pressure coefficient $\bar{C}_p$ on the upper wing surface with respect to iteration number at $\alpha = 3.5°$ for a straight wing of aspect ratio $\mathcal{R} = 3$; subplots (a) through (d) ordered by increasing iteration number, specifically 10 000, 40 000, 60 000 and 120 000 iterations.
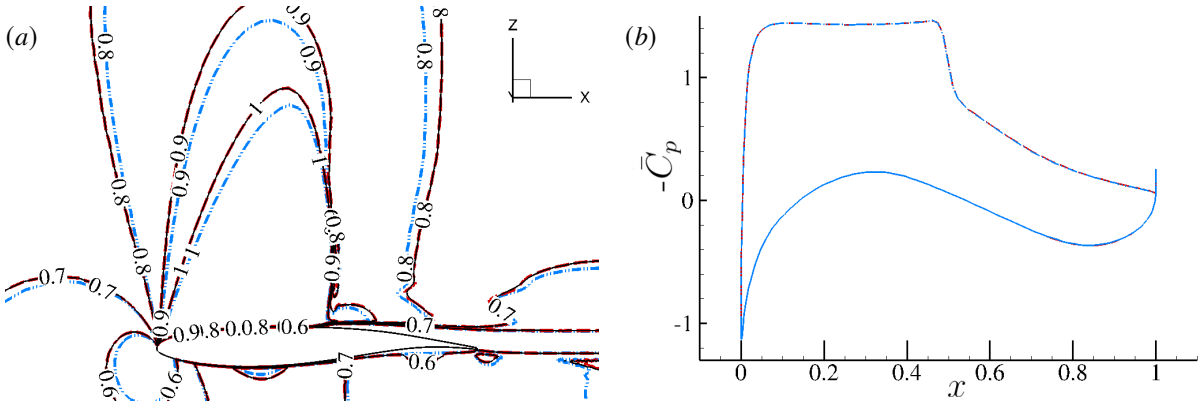

Fig. 6 Comparison of (a) Mach lines from two-dimensional aerofoil (black lines) as well as three-dimensional parallel flow on infinite straight wing (red) and $\Lambda = 20°$ swept wing (blue) at $\alpha = 3.5°$ and (b) corresponding normalized pressures coefficient $\bar{C}_p$.

1. Straight Wing Parallel Flow

For $\alpha = 3.2°$ and $3.3°$ straight wing cases, the simulations quickly converge to the defined level of 10^{-12}. There is no three-dimensional cellular flow pattern visible on the wing surface as shown in fig. 3. Interestingly, when increasing the angle of attack, the iteration count is substantially higher for $\alpha = 3.4°$. This suggests that we are in the vicinity of a critical condition and it takes more iterations to amplify the spanwise-periodic mode with positive growth rate close to zero. This statement will be verified in Sec. IV.A by using stability theory to extract dominant eigenmodes.

Taking $\alpha = 3.5°$ as an example, the simulation shows no three-dimensional cellular pattern until about 10 000 iterations (see fig. 5(a)), which describes the first linear convergence trend in fig. 4(a). Although this type of parallel flow is found at a residual level $R_\rho \approx O(10^{-8})$, it is still two orders of magnitude lower compared to typical convergence levels used in industrial RANS simulations. Figure 6(a) demonstrates the parallel nature of the flow at 10 000 iterations by comparing Mach lines in the xz-plane for the straight and a swept wing at $20°$ sweep angle to the pure two-dimensional aerofoil flow at the same flow conditions (in a plane normal to the wing leading edge). Excellent agreement is found between the straight wing and the aerofoil flow. Hence, it is reasonable to assume an initial parallel flow on the straight infinite wing. It can also be seen that the sonic zone contracts for the swept wing flow. Even though the leading-edge normal reference velocity is made equal independent of sweep angle, the flow fields are not identical in the plane. However, the corresponding surface pressure coefficients $\bar{C}_p$ using normalised reference values in the xz-plane are identical. Continuing the steady-state iterations for the case in fig. 5, the flow enters a stage where disturbances seem to grow. Here, the three-dimensional flow field is formed, as seen starting from 40 000 iterations in fig. 5(b). This continues until non-linear saturation helps establishing the final steady state.
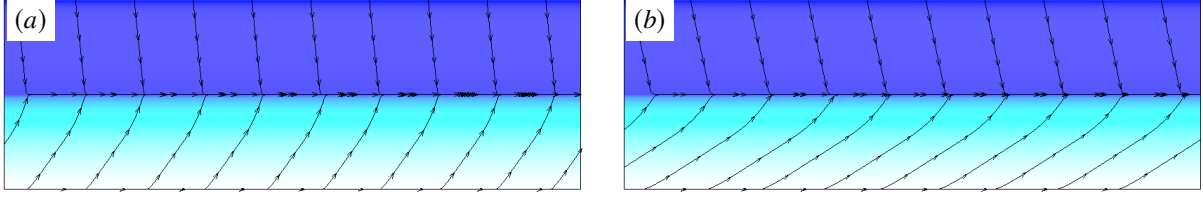
Fig. 7 **Surface pressure coefficient $\bar{C}_p$ on the upper wing surface of (*a*) $\Lambda = 10°$ and (*b*) $20°$ swept flows. Normalisation is based on reference values in plane normal to the leading edge.**
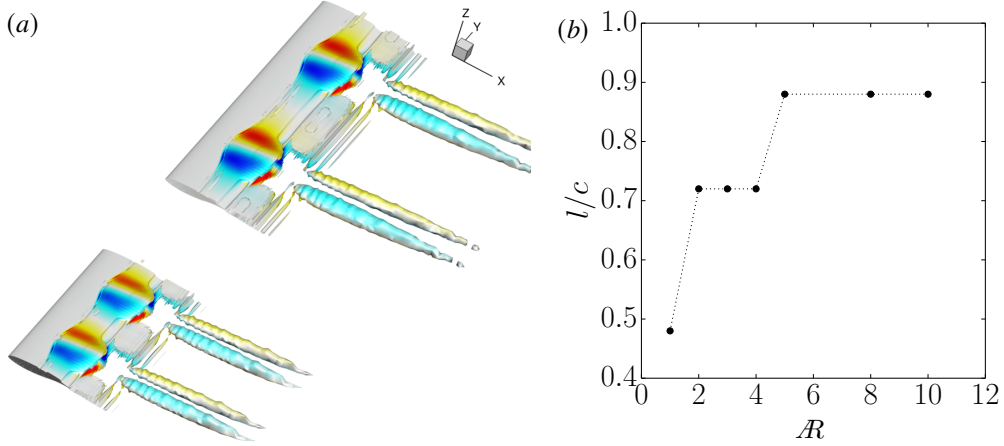

Fig. 8 **Three-dimensional structures on upper surface of straight wings with $A\!R = 3$ and 5 at $\alpha = 3.5°$ visualised by Q-criterion of value 0.05 coloured by spanwise velocity (*a*), and cell size varying with aspect ratio (*b*).**

2. Swept Wing Parallel Flow

When the freestream direction is not perpendicular to the leading edge of the wing, flow over a swept wing is described. Following eq. (1), we ensure that the flow conditions normal to the leading edge are constant, independent of the sweep angle. Different sweep angles are discussed herein, specifically $\Lambda = 5°$, $10°$ and $20°$. Their convergence behaviour is compared to the straight wing in fig. 4(*b*). The density residual is well converged for $\Lambda = 20°$ and, interestingly and in contrast to the straight wing, spanwise-parallel flow is formed at terminal convergence. At the lower sweep angles of $\Lambda = 5°$ and $10°$, convergence stalls, failing to reach the specified tolerance, and different methods, such as selective frequency damping [28], should be explored in the future to find fully converged base flow. Close inspection of the corresponding non-converged flow field suggests indecisiveness in either forming spanwise cellular structures as for $\Lambda = 0°$ or converging towards spanwise parallel flow as for $\Lambda = 20°$. However, similar to the discussion for the straight wing above, parallel flow is identified at $R_\rho \approx O(10^{-8})$. Figure 7 presents the normalised surface pressure coefficient C_p and surface skin-friction lines for the flows at $\Lambda = 10°$ and $20°$. Since the parameters α, $Re_{\infty,n}$ and $M_{\infty,n}$ are the same, and identical to the straight wing, the flow in that plane normal to the leading edge is similar.

3. Straight Wing Non-Parallel Flow

Based on previous investigations[5, 29], three-dimensional spanwise cellular patterns exist in post-onset shock-buffet conditions for the straight wing of aspect ratio $A\!R = 3$. Again, taking $\alpha = 3.5°$ as an example, the simulation starts to show three-dimensional cellular patterns after 40 000 iterations with $R_\rho = (10^{-5})$ (see fig. 5(*b*)). The pronouncedness of cells continues to grow while the residual goes down, until the flow reaches the stage of nonlinear saturation, where the flow appears to describe the spanwise-periodic non-oscillatory mode discussed by Crouch et al. [1]. Figure 8(*a*) presents the three-dimensional flow field on two wings of aspect ratios $A\!R = 3$ and 5. The figure shows that each cell comes with a pair of counter-rotating trailing vortices. Figure 8(*b*) illustrates the size of each cell, where l/c measures the distance between its two foci) varying with aspect ratio. A more detailed study is given in the appendix for different aspect ratio wings between $A\!R = 1$ and 10.
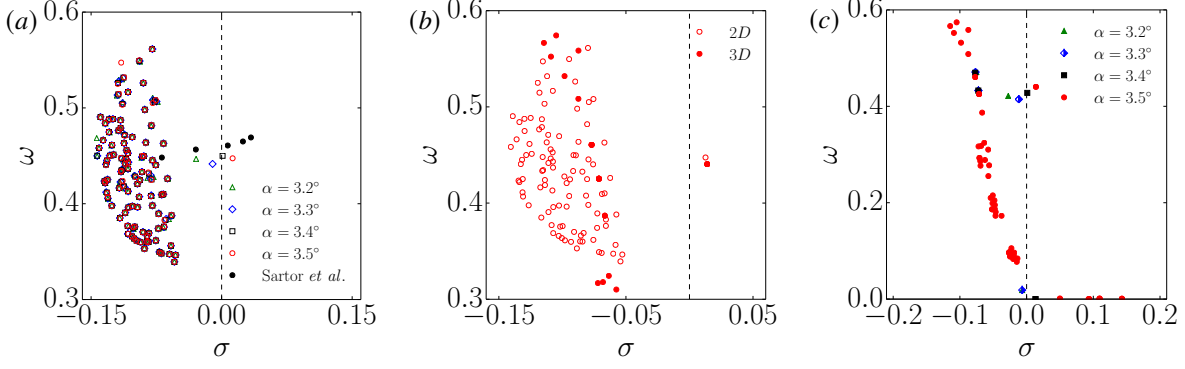
7

Fig. 9 Eigenspectra of stability problem in (*a*) two-dimensional (2D) flow, (*b*) comparison between two-dimensional and three-dimensional (3D) parallel flow, and (*c*) three-dimensional parallel flow.
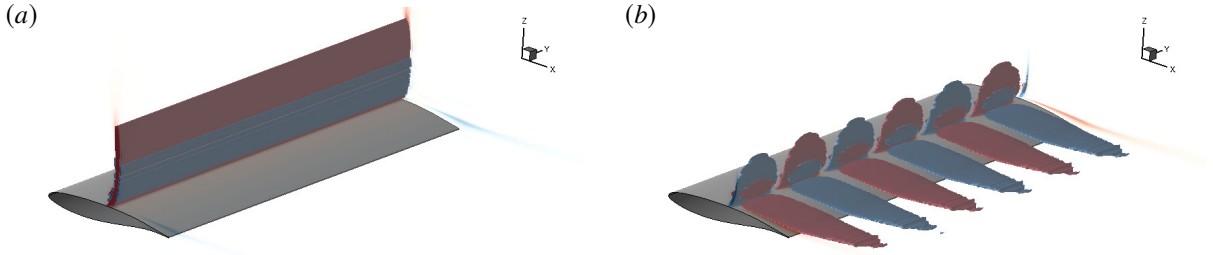

Fig. 10 Real part of total energy amplitude $\widehat{\rho E}$ of the spanwise-uniform (aerofoil) oscillatory mode in (*a*) and the leading spanwise-periodic monotone stationary mode in (*b*) at $\alpha = 3.5°$. Eigenvectors are normalised by their respective maximum amplitude $\widehat{\rho E}$. The plots show the volumetric iso-surfaces at values ±0.1.

IV. Triglobal Stability Results

A wide range of (essentially continuous) wavenumbers can be scrutinised in the framework of biglobal stability analysis. Hence, modes with (very) long, intermediate and short wavelengths have been found. Crouch et al. [1] contemplate the physical meaning of those short wavelength modes in the context of turbulence modelling, due to the spanwise length scales becoming similar to the shear layer thickness. At the same time, in a triglobal analysis, very long (albeit wavenumber $\beta \neq 0$) and very short wavelength modes quickly become computationally prohibitive; very small wavenumbers require a high aspect ratio, whereas very large wavenumbers require small spanwise grid spacings.

A. Triglobal Instability of Straight Wing Parallel Flow

We start by carrying out a two-dimensional aerofoil stability analysis computing eigenvalues at angles of attack between $\alpha = 3.2°$ and $3.5°$. In fig. 9(*a*), our results are compared with the work by Sartor et al. [4] showing their eigenvalues in the range $\alpha = 3°$ to $4°$ in increments of $0.25°$, highlighted by solid black dots (●). To be unambiguous, two-dimensional stability analysis refers to a two-dimensional aerofoil mesh and using both a two-dimensional base flow and perturbation ansatz, with no spanwise component considered whatsoever. Specifically, the perturbation around the base flow takes the form $\hat{u}(x, y)\, e^{\lambda t}$, where $\hat{u}$ is the complex-valued amplitude function of the five conservative variables (excluding spanwise momentum) on a two-dimensional mesh defined by (x, y). The perturbation is stable for angles of attack $\alpha < 3.4°$. At approximately $\alpha = 3.4°$, the decay rate ($\sigma < 0$) turns into a growth rate ($\sigma > 0$) with the leading eigenvalue crossing the imaginary axis into the positive half plane, which means the perturbation is marginally unstable growing exponentially in time. Note that differences in onset angle of attack compared with previous work on the same aerofoil can be explained by the slight change of the S-A turbulence model. Specifically, in [1, 2] the so-called compressibility correction [30] is added as additional term, which is not included herein. The effect of this correction is a lowering of eddy-viscosity levels promoting an earlier onset of the instability. On the contrary, Sartor et al. [4] predict the onset angle of attack at approximately $\alpha = 3.4°$, similar to our work, without using the correction term. Interestingly, the wind tunnel test data in Jacquin et al. [5], using the same aerofoil and flow conditions, agree more
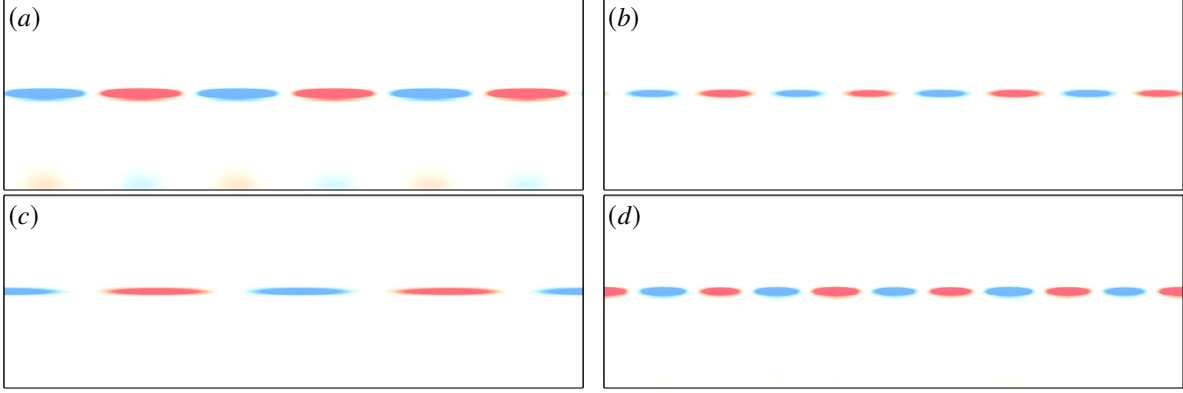
Fig. 11 Surface pressure coefficient $\widehat{C}_p$, plotted in range $[-0.001, 0.001]$, of unstable spanwise-periodic monotone modes (ordered with decreasing growth rate as seen in fig. 9(c)) for infinite straight wing at $\alpha = 3.5°$

closely with the numerically predicted lower shock-buffet onset angle of attack. At $\alpha = 3.5°$, strong shock unsteadiness dominates the entire flow, and there is one single unstable buffet mode with an angular frequency $\omega = 0.44$ (equivalent to a Strouhal number $St \equiv \omega/(2\pi) \approx 0.07$), which is close to the experimental value for the same aerofoil [5] and agrees with the frequencies typically reported for aerofoil shock buffet. Instead for triglobal analysis, the perturbation around the base flow takes the form $\hat{\boldsymbol{u}}(x, y, z)\, e^{\lambda t}$, with vector $\hat{\boldsymbol{u}}$ now having six variables (five for the RANS equations and one for the turbulence model) per mesh point. The primary purpose of this discussion is to validate the ability of the method to solve the three-dimensional linearised system with a spanwise periodic boundary condition. The stability results on the wing with aspect ratio $\mathcal{R} = 3$ using parallel base flow at angle of attack $\alpha = 3.5°$ is selected to compare with the two-dimensional eigenspectrum, as seen in fig. 9(b). Note, albeit using the same two-dimensional mesh (which is extruded to create the infinite wing) and finding good agreement overall, remaining differences in the critical eigenvalue can be explained, for instance, in that the parallel base flow for the infinite wing is approximate and the influence of modelled aspect ratio needs further scrutiny.

Importantly, the migration of a dominant triglobal spanwise-uniform oscillatory mode can be observed while incrementing the angle of attack, see fig. 9(c). At angles of attack $\alpha = 3.2°$ and $3.3°$, the flow is globally stable, and the modes' spatial structures are spanwise uniform. This agrees with the results of the fully converged steady-state RANS simulations shown in fig. 3. As the angle of attack is increased, the spanwise-uniform mode becomes unstable just below $\alpha = 3.4°$ with angular frequency $\omega = 0.44$ and growth rate nearly identical to the aerofoil analysis. The spatial structure of this nominally aerofoil mode at angle of attack $\alpha = 3.5°$ is visualised in fig. 10(a), showing the real part of the spatial amplitude function of the total energy $\widehat{\rho E}$, highlighting the synchronisation between the shock oscillation and the resulting pulsating shear layer. The eigenvector has been normalised by the maximum modulus of the energy perturbation. Besides the oscillatory aerofoil mode, four spanwise-periodic monotone (i.e. with zero frequency) stationary modes are identified. The leading unstable monotone mode at $\alpha = 3.5°$, shown in fig. 10(b), has three cells each with a non-dimensional spanwise wavelength $L = 1$ (corresponding to a wavenumber $\beta \equiv 2\pi/L = 2\pi$), measured parallel to the leading edge. Note that the periodic boundary condition only permits an integer number of cells for a given aspect ratio. For the $\mathcal{R} = 3$ case shown, this corresponds to the wavenumber varying between $\beta = {}^4/_3\,\pi$ and ${}^{10}/_3\,\pi$ for the four modes. All modes are visualised in fig. 11 showing the cellular pattern on the wing surface highlighted by the pressure coefficient $\widehat{C}_p$. Note that at angle of attack $\alpha = 3.4°$, both the spanwise-uniform and spanwise-periodic modes are marginal, explaining the very slow full convergence indicated in fig. 4(a).

B. Triglobal Instability of Swept Wing Parallel Flow

In previous biglobal studies on infinite wings [1, 2], the frequency range of dominant modes related to the shock-buffet instability in global stability studies on swept wings was found to be up to an order of magnitude higher compared with the aerofoil mode on a straight wing, depending on the particular flow configuration, specifically sweep angle. Figure 12 presents the eigenspectra resulting from the stability analysis on wings with sweep angles between $\Lambda = 0°$ and $20°$. Besides observing the spanwise-uniform (aerofoil) oscillatory mode, the spanwise-periodic monotone stationary modes on the straight wing become oscillatory travelling modes for non-zero sweep angles, as reported in previous
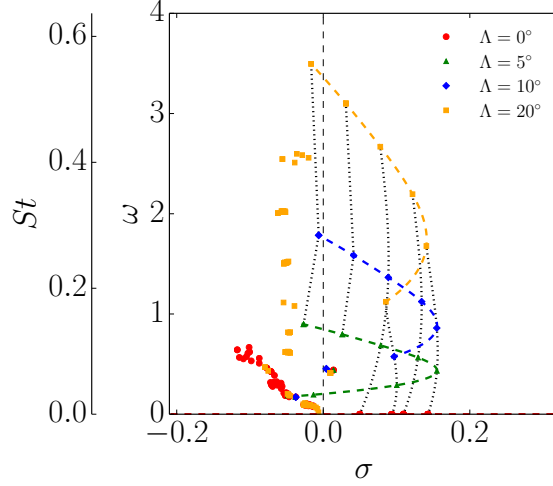
Fig. 12 Eigenspectra of parallel flow cases with different sweep angles between $\Lambda = 0°$ and $20°$ at $\alpha = 3.5°$.
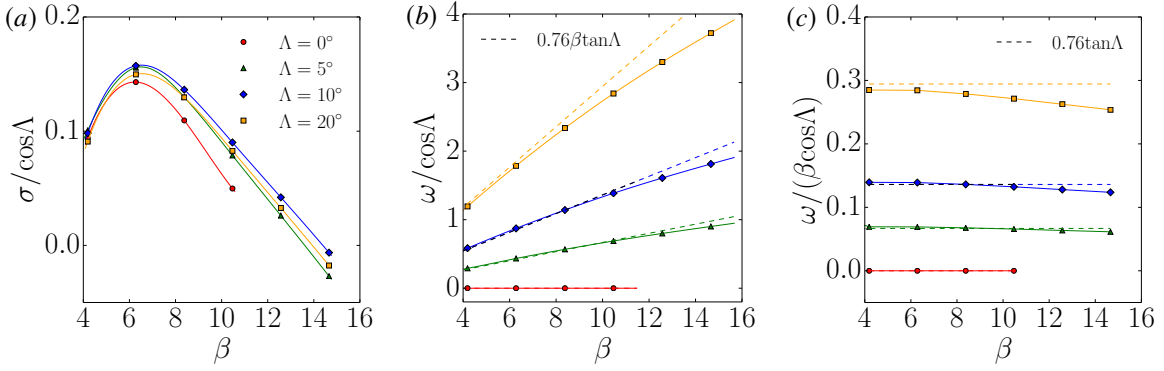

Fig. 13 Growth rate (*a*), angular frequency (*b*) and phase speed (*c*) (all normalised by reference velocity normal to leading edge and chord length) as a function of wavenumber β.

biglobal studies. As a general trend, the oscillation frequency increases with the sweep angle. Also, for a given sweep angle, the oscillation frequency increases with the number of cells along the span. Taking the wing with $\Lambda = 20°$ as an example, its dominant modes cover a broadband frequency range between $\omega \approx 1$ and 4 (corresponding to Strouhal numbers between $St \approx 0.16$ and 0.65).

To comprehend the effect of sweep angle, results scaled by the velocity in the plane normal to the leading edge are presented in fig. 13, which characterises the spanwise-periodic modes by showing growth rate, angular frequency and speed of propagation as a function of wavenumber β. In fig. 13(*a*) it can be seen clearly that the highest growth rate is found for the modes with wavenumber approximately $\beta = 2\pi$, corresponding to a wavelength $L = 1$ (i.e. three cells for $A\!R = 3$, for both the straight and swept wings. The normalised growth rate only changes slightly with sweep angle (albeit showing an increase from the straight wing flow). The frequency of the unstable modes grows both with the wavenumber and sweep angle, as shown in fig. 13(*b*). Previously, the empirical relation, $\omega/\cos\Lambda = 0.76\,\beta\tan\Lambda$, has been presented in Paladini et al. [2]. Note that for consistency in notation, we refer to reference values in a plane normal to the leading edge. Overall good agreement is found. As observed in experiments on finite swept wings, three-dimensional (so-called) buffet cells propagate outboard along the span. The non-dimensional phase speed of those modes can be given by the empirical relation, $\omega/(\beta\cos\Lambda) = 0.76\tan\Lambda$, hence increasing with sweep angle. In the range $\beta < 16$ examined here, the phase speed is nearly constant for each sweep angle, see fig. 13(*c*). Finally, the spanwise-periodic oscillatory travelling modes visualising the real part of the surface pressure coefficient $\widehat{C}_p$ are shown in fig. 14. The imaginary part (not shown therein) is spatially $90°$ out of phase, i.e. minima and maxima can be found at zero crossings of the corresponding real part, to allow the spanwise propagation of cells.
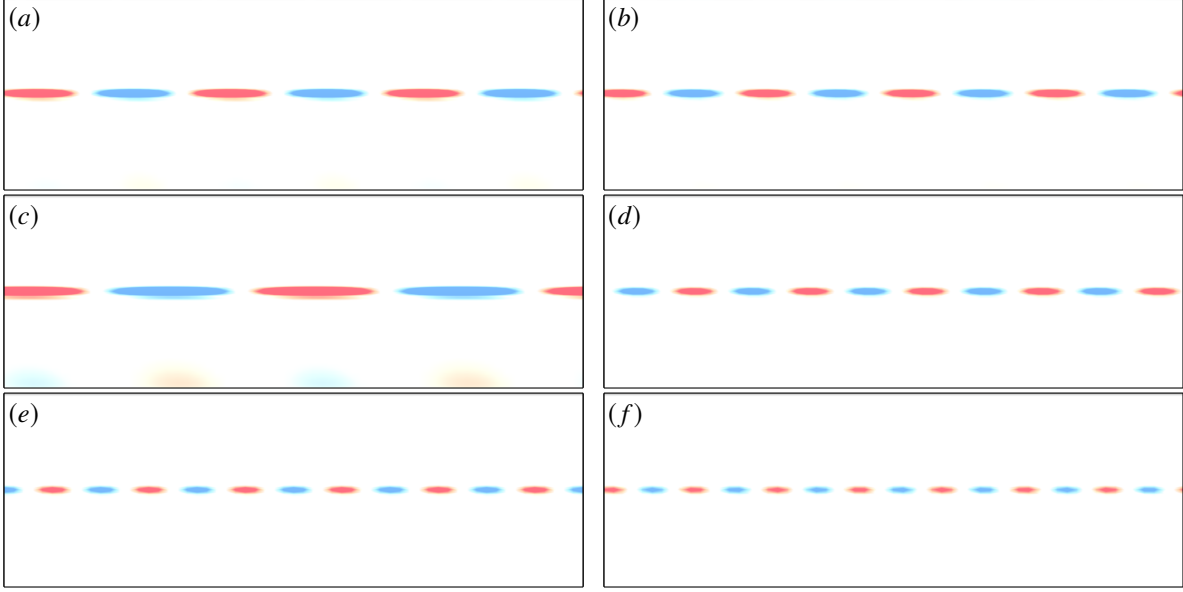
Fig. 14 Real part of surface pressure coefficient $\widehat{C}_P$, plotted in range $[-0.001, 0.001]$, of spanwise-periodic oscillatory outboard-travelling modes (ordered with decreasing growth rate as seen in fig. 12) for infinite wing with sweep angle $\Lambda = 20°$ at $\alpha = 3.5°$.

C. Triglobal Instability of Straight Wing Non-Parallel Flow

Attention now turns towards the non-parallel base flow obtained at terminal convergence of the steady RANS iterations. We focus on analysing the stability of the straight wing whose base flow contains three-dimensional cellular structures, as shown e.g. figs. 3 and 8. The wings with $\mathcal{R} = 3$ and 5 were chosen to represent the short and long wings on account of the cell size characteristics studied in the Appendix. Figure 15 shows the eigenspectra of these two wing flows at $\alpha = 3.5°$. In the small aspect ratio wing, one single unstable mode is identified with a frequency $\omega \approx 0.4$, close to the spanwise-uniform (aerofoil) mode's frequency in parallel flow. There is also a marginal mode with a slightly decreased frequency. These two modes are proper three-dimensional. Spatial amplitudes follow the shock structure of the base flow. For the unstable mode the dynamics of the two cells are synchronised (see fig. 16(a)), whereas for the marginal mode the cells are out of phase (see fig. 16(b)). To confirm accuracy of the eigensolution, a comparison with time-marching unsteady RANS is shown in fig. 17. Figure 17(a) shows the lift coefficient perturbation around the base flow, $\widetilde{C}_L = C_L - \bar{C}_L$. The reconstruction of the unsteady flow solution from the global mode makes use of the relation $\widetilde{C}_L(t) = \widehat{C}_L\, e^{\lambda t} + c.c.$, where $c.c.$ refers to complex conjugate. From the figure, we can see that the stability tool produces results on a par with time-marching unsteady RANS. For $\mathcal{R} = 3$ in fig. 17(a), unsteady RANS simulations are shown starting both from parallel and non-parallel base flows, respectively. Note that the perturbation is taken in both cases with respect to the non-parallel base flow. The global stability analysis can predict the linear growth of the perturbation until about $t \approx 0.4$ (see fig. 18(a)), before a non-linear mechanism plays the dominant role in saturating the growth. Figure 18(c) and (d) show a limit-cycle oscillation (LCO) of the spanwise-uniform shock front corresponding to the expansion and contraction of its downstream shear layer (essentially a two-dimensional aerofoil behaviour). In the linear growth stage ($0 < t < 0.4$), the Strouhal number is 0.06, which is in agreement with the frequency given by the non-parallel stability analysis. Furthermore, in the LCO stage ($t > 0.6$), the Strouhal number increases slightly.

In the case of the larger aspect ratio wing, two unstable modes are observed. The growth rate of the leading mode is lower compared to the shorter $\mathcal{R} = 3$ wing, while its frequency is slightly increased. The spatial structures of the modes are similar to those on the $\mathcal{R} = 3$ wing, as shown in fig. 16(c) and (d). Looking at the long time history from unsteady RANS in fig. 17(b), these two unstable modes seem to act together causing more irregular lift fluctuations, and a destruction of the otherwise spanwise-uniform flow pattern on the $\mathcal{R} = 3$ wing. A cause could be a cancellation of the shock curvature resulting from the out-of-phase spatial structures shown in fig. 16(c) and (d). Unsteady RANS for this case starts from the well converged non-parallel flow containing the shock buffet cells (see fig. 20). It takes some time within the linear growth stage to amplify the buffet cells before entering into a limit-cycle oscillation at $t \approx 0.54$. At this stage ($0.7 < t < 1.4$), the flow becomes nominally two dimensional featuring a strong shock oscillation with $St \approx 0.07$
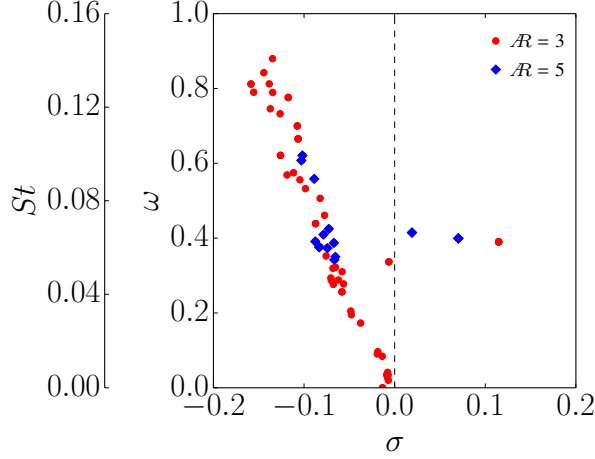
11

Fig. 15   Comparison of eigenspectra for $Æ = 3$ and 5 straight wing non-parallel flow at $\alpha = 3.5°$
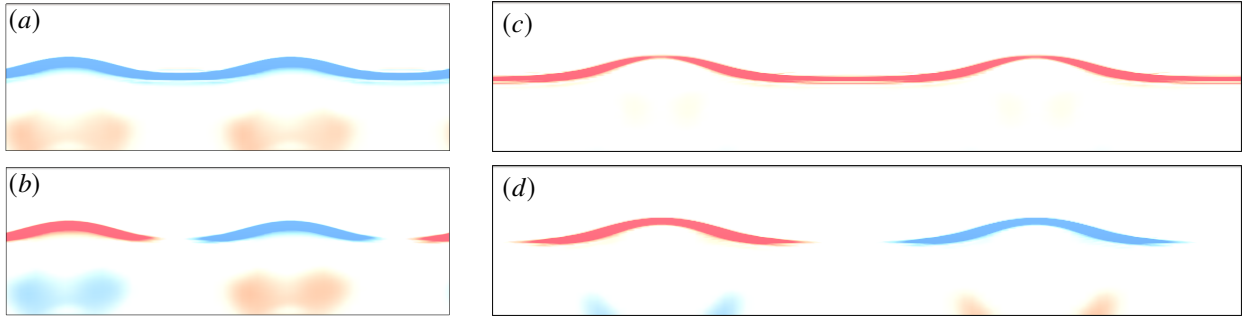

Fig. 16   Real part of surface pressure coefficient $\widehat{C}_P$ plotted in range $[-0.001, 0.001]$ of the leading (a, c) and the second marginal (b, d) modes of the non-parallel flow for $Æ = 3$ and 5 straight wings.
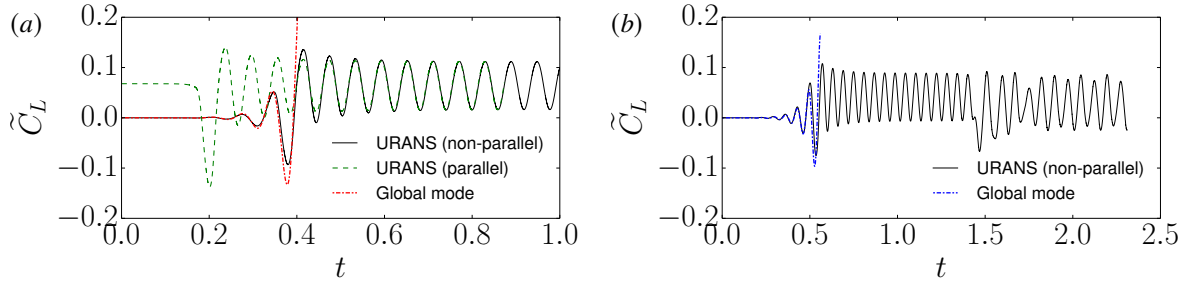

Fig. 17   Time histories of unsteady lift coefficient perturbation $\widetilde{C}_L$ calculated by unsteady RANS (URANS) and linear global mode for (a) $Æ = 3$ and (b) $Æ = 5$ at $\alpha = 3.5°$.

(fig. 18(f)). At around $t = 1.45$, cells of different wavelengths appear and distort the spanwise-uniform flow pattern (fig. 18(g)). Finally, these two cells merge together and leave one cell oscillating (fig. 18(h)), in addition to the whole shock front moving along the chord. Interestingly, in the parallel LCO stage of the two unsteady RANS simulations the lift oscillations not only have the same frequency, but also the same mean lift coefficient of 0.976 and oscillation amplitude. This implies that, using a small aspect ratio wing with proper periodic boundary condition, unsteady RANS can describe the motion associated with aerofoil shock buffet on the infinite wing, before it fails to predict the final irregular behaviour on the larger aspect ratio wing. Since the $Æ = 5$ wing has a higher base-flow lift coefficient, $\bar{C}_L = 0.9329$, its shift towards the mean-flow value in the parallel LCO stage is lower compared to the $Æ = 3$ wing.
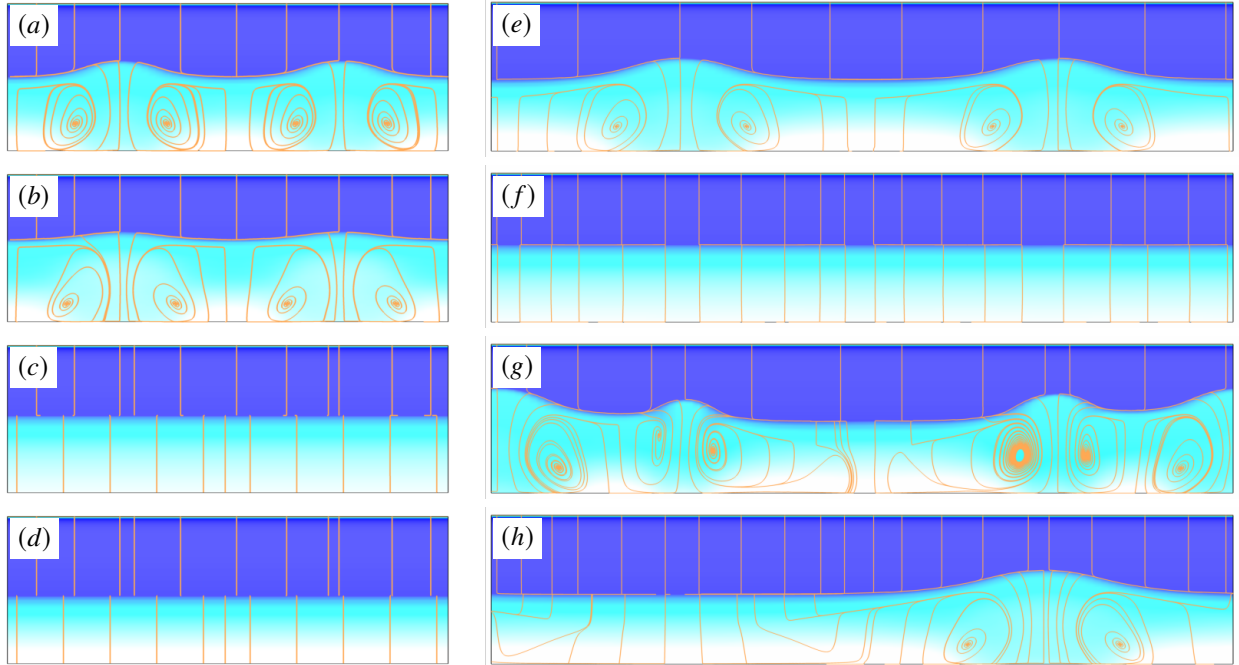
Fig. 18 **Snapshots of surface pressure coefficient C_p, plotted in range [-1,1], for $\mathcal{R} = 3$ at dimensionless time (in fig. 17(a)) $t = 0.3,\ 0.4,\ 0.64,\ 0.68$ ((a) – (d)) and $\mathcal{R} = 5$ at dimensionless time (in fig. 17(b)) $t = 0.4,\ 0.9,\ 1.45,\ 2.1$ ((e) – (h)). Both unsteady RANS simulations start from non-parallel base flow on the straight wing.**

V. Conclusions

Triglobal stability analysis of infinite wings featuring shock buffet is performed on two types of base flow; parallel (with reference to the leading edge) flow on straight and swept wings and non-parallel flow on a straight wing. Infinite wing flow is imposed using a spanwise periodic boundary condition, which was linearised in the chosen flow solver as part of the current study. Spanwise flow gradients are permitted when computing the steady base flow, which generalises the more restrictive spanwise-uniform assumption of biglobal analysis. Swept wing flow is simulated by adjusting the freestream velocity to ensure the reference variables in the plane perpendicular to the leading edge of the wing are constant. The straight and swept wing parallel (spanwise-uniform) base flows, studied at angles of attack around the onset of shock buffet, are nominally two dimensional without spanwise cellular structures. The base-flow results are quantitatively comparable to a pure two-dimensional aerofoil analysis, albeit using a fully three-dimensional solution approach in our study. Besides a spanwise-uniform (aerofoil) oscillatory mode, four discrete spanwise-periodic monotone stationary modes are found. These monotone modes develop into oscillatory travelling modes in swept-wing flow covering a typical broadband frequency range. The highest growth rates independent of sweep angle are found for a spanwise wavenumber of approximately 2π, corresponding to a wavelength of one chord. The frequency and phase speed increase with the sweep angle and agree with an empirical relation previously established. While the frequency of a discrete mode increases with wavenumber, the phase speed is independent thereof. In the non-parallel straight wing flow, only one discrete unstable mode can be identified on the wing with $\mathcal{R} = 3$. The second, marginal mode in the $\mathcal{R} = 3$ case becomes unstable in $\mathcal{R} = 5$ wing flow. Good agreement is found between the computed eigenmodes and unsteady time-marching results to predict the perturbation characteristics. The two unstable modes in the larger aspect ratio wing seem to interact with each other to modify the otherwise spanwise-uniform oscillating flow into a more irregular three-dimensional oscillatory type. The underlying mechanism needs to be scrutinised in future work.

Appendix — Convergence Studies

A convergence study is performed to assess the impact of the grid resolution in the spanwise direction. Five grids of a wing with aspect ratio $\mathcal{R} = 3$ are considered at a fixed angle of attack $\alpha = 3.5°$, featuring a uniform spanwise spacing using between 15 and 120 points giving $\Delta y = 0.2$ to 0.025. The lift and drag coefficients of the converged flow

Table 2 Mesh convergence study at $\alpha = 3.5°$ for wing with $Æ = 3$.

n_y	Δy	$\bar{C}_L$	$\bar{C}_D$
15	0.2	0.978026	0.045550
30	0.1	0.943001	0.044595
60	0.05	0.910152	0.043981
90	0.033	0.909382	0.043988
120	0.025	0.910180	0.044011
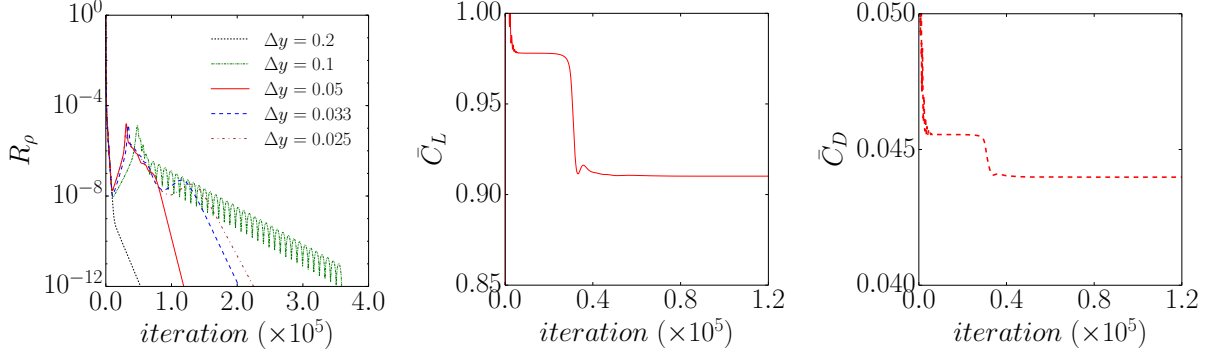
Fig. 19 Convergence history of density residual norm for different spanwise spacings (left) and force coefficients using $\Delta y = 0.05$ (middle and right) at $\alpha = 3.5°$.

solution are summarised in table 2. We can see that using 60 points altogether (20 points per unit length of span) is required and sufficient, introducing an error of less than 0.01% as estimated by the lift coefficient $\bar{C}_L$ compared with the finest mesh $n_y = 120$. Similarly, from the comparison of the density residual norm R_ρ over iterations for different mesh resolutions in fig. 19 (left), we can see the impact on the formation of the cellular pattern at the fixed angle of attack. Effectively, a minimum mesh resolution is required to capture the spanwise cellular flow pattern. Overall, $\Delta y = 0.05$ was selected for the majority of results presented. The history of lift and drag coefficients ($\bar{C}_L$ and $\bar{C}_D$) over iterations is also shown in the figure for the resolution with $\Delta y = 0.05$. It can be seen that step changes in the coefficients agree with the corresponding convergence behaviour. Also compare with the corresponding surface flow development in fig. 5.

Figure 20 shows fully converged steady RANS results. It can be seen that a single cell (outlined by skin friction lines) forms on the wings with $Æ = 1$ and 2. Then, two cells can be observed on the wing with $Æ = 3$, which is consistent with the findings in the OAT15A experiment [5]. In contrast, in the numerical simulations using the OALT25 aerofoil [29] the two-cell pattern of transonic buffet can only be observed when $Æ > 4.52$. Twin cells also exist for medium spans of $Æ = 5$. However, in larger aspect ratio wings with $Æ = 8$ and 10, the cell number is increased to three. However, to the authors' knowledge, previous work has not clearly pointed out the connection between spanwise cell size and wing aspect ratio. Here, an aspect-ratio influence on the size of each cell can be observed. The size of a three-dimensional cellular pattern is defined by the length l (highlighted by dashed line in fig. 20) between two foci of a single cell, as shown also in fig. 8. A small value of $l/c = 0.48$ (where c is the chord length) is measured for $Æ = 1$, which suggests that such a small physical domain in the spanwise direction is not sufficient, despite imposing periodic boundary condition. One interesting point to note is that the length nearly remains constant at $l/c = 0.72$ when $Æ \leqslant 4$, increasing to $l/c \approx 0.9$ for larger aspect ratios (see fig. 8(b)).
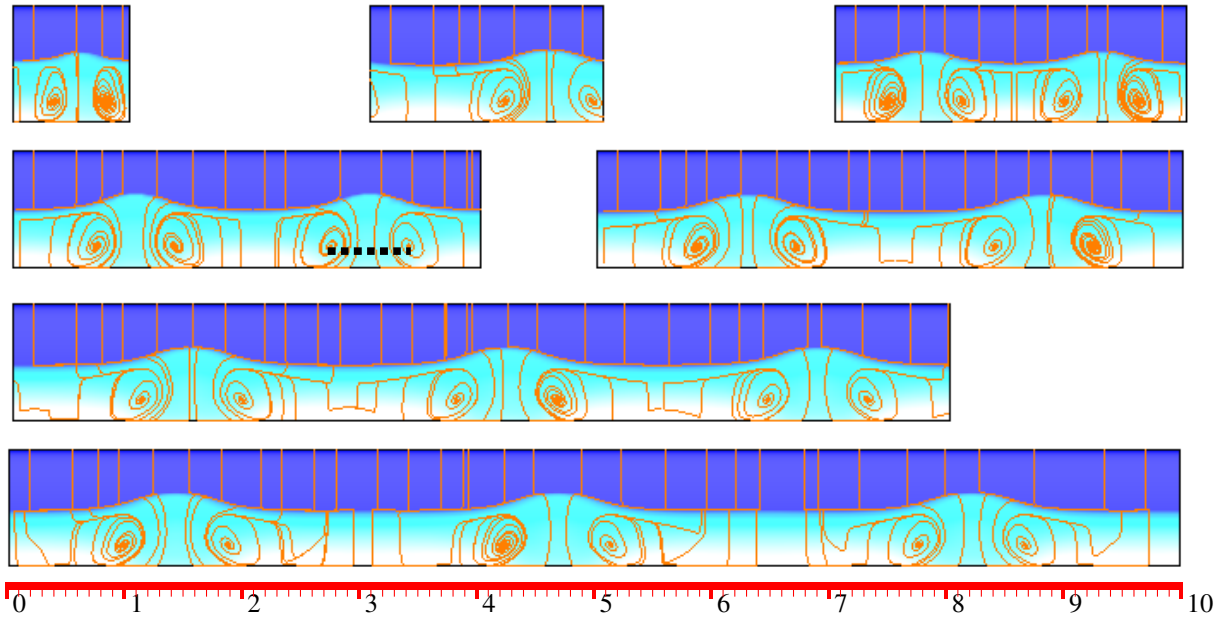
Acknowledgments

Fig. 20   Steady base flow surface pressure coefficient $\bar{C}_p$ as a function of $\mathit{\!R}$ at $\alpha = 3.5°$.

References

[1] Crouch, J. D., Garbaruk, A., and Strelets, M., "Global Instability in the Onset of Transonic-Wing Buffet," *Journal of Fluid Mechanics*, Vol. 881, 2019, pp. 3–22. doi:10.1017/jfm.2019.748.

[2] Paladini, E., Beneddine, S., Dandois, J., Sipp, D., and Robinet, J.-C., "Transonic Buffet Instability: From Two-dimensional Airfoils to Three-Dimensional Swept Wings," *Physical Review Fluids*, Vol. 4, 2019, p. 103906. doi:10.1103/PhysRevFluids.4.103906.

[3] Plante, F., Dandois, J., Beneddine, S., Sipp, D., and Laurendeau, E., "Numerical Simulations and Global Stability Analyses of Transonic Buffet and Subsonic Stall," *AAAF AERO2019*, hal–02127307, Paris, France, 2019.

[4] Sartor, F., Mettot, C., and Sipp, D., "Stability, Receptivity, and Sensitivity Analyses of Buffeting Transonic Flow over a Profile," *AIAA Journal*, Vol. 53, No. 7, 2015, pp. 1980–1993. doi:10.2514/1.J053588.

[5] Jacquin, L., Molton, P., Deck, S., Maury, B., and Soulevant, D., "Experimental Study of Schock Oscillation over a Transonic Supercritical Profile," *AIAA Journal*, Vol. 47, No. 9, 2009, pp. 1985–1994. doi:10.2514/1.90190.

[6] Rodríguez, D., and Theofilis, V., "On the Birth of Stall Cells on Airfoils," *Theoretical and Computational Fluid Dynamics*, Vol. 25, No. 1–4, 2011, pp. 105–117. doi:10.1007/s00162-010-0193-7.

[7] He, W., Gioria, R. S., Pérez, J. M., and Theofilis, V., "Linear Instability of Low Reynolds Number Massively Separated Flow around Three NACA Airfoils," *Journal of Fluid Mechanics*, Vol. 811, 2017, pp. 701–741. doi:10.1017/jfm.2016.778.

[8] Bippes, H., and Turk, M., "Windkanalmessungen in Einem Rechteckflügel bei Anliegender und Abgelöster Strömung," Tech. Rep. IB251-80A18, DFVLR Forschungsbericht, 1980.

[9] Winkelmann, A., and Barlow, B., "Flowfield Model for a Rectangular Planform Wing beyond Stall," *AIAA Journal*, Vol. 8, 1980, pp. 1006–1008. doi:10.2514/3.50846.

[10] Weihs, D., and Katz, J., "Cellular Patterns in Post Stall Flow over Unswept Wings," *AIAA Journal*, Vol. 21, No. 12, 1983, pp. 1757–1759. doi:10.2514/3.8321.

[11] Yon, S. A., and Katz, J., "Study of the Unsteady Flow Features on a Stalled Wing," *AIAA Journal*, Vol. 36, No. 3, 1998, pp. 305–312. doi:10.2514/2.372.

[12] Barakos, G., and Drikakis, D., "Numerical simulation of transonic buffet flows using various turbulence closures," *International Journal of Heat and Fluid Flow*, Vol. 21, No. 5, 2000, pp. 620–626. doi:https://doi.org/10.1016/S0142-727X(00)00053-9.

15

[13] Garbaruk, A., Shur, M., Strelets, M., and Spalart, P. R., "Numerical Study of Wind-Tunnel Walls Effects on Transonic Airfoil Flow," *AIAA Journal*, Vol. 41, No. 6, 2003, pp. 1046–1054. doi:10.2514/2.2071.

[14] Thiery, M., and Coustols, E., "Numerical Prediction of Shock Induced Oscillations over a 2D Airfoil: Influence of Turbulence Modelling and Test Section Walls," *International Journal of Heat and Fluid Flow*, Vol. 27, 2006, pp. 661–670. doi:10.1016/j.ijheatfluidflow.2006.02.013.

[15] Crouch, J. D., Garbaruk, A., and Magidov, D., "Predicting the Onset of Flow Unsteadiness Based on Global Instability," *Journal of Computational Physics*, Vol. 224, No. 2, 2007, pp. 924–940. doi:10.1016/j.jcp.2006.10.035.

[16] Mcdevitt, J. B., and Okuno, A. F., "Static and Dynamic Pressure Measurements on a NACA 0012 Airfoil in the Ames High Reynolds Number Facility," Tech. Rep. TP–2485, NASA, 1985.

[17] Iorio, M. C., González, L. M., , and Ferrer, E., "Direct and Adjoint Global Stability Analysis of Turbulent Transonic Flows over a NACA0012 P rofile," *International Journal for Numerical Methods in Fluids*, Vol. 76, No. 3, 2014, pp. 147–168. doi:10.1002/fld.3929.

[18] Timme, S., and Thormann, R., "Towards Three-Dimensional Global Stability Analysis of Transonic Shock Buffet," *AIAA Atmospheric Flight Mechanics Conference*, AIAA Paper 2016–3848, Washington, D.C., 2016. doi:10.2514/6.2016-3848.

[19] Timme, S., "Global Instability of Wing Shock Buffet," *arXiv eprint arXiv:1806.07299*, 2018.

[20] Timme, S., "Global Shock Buffet Instability on NASA Common Research Model," *AIAA Scitech 2019 Forum*, AIAA Paper 2019–0037, San Diego, California, 2019. doi:10.2514/6.2019-0037.

[21] Masini, L., Timme, S., and Peace, A., "Analysis of a Civil Aircraft Wing Transonic Shock Buffet Experiment," *Journal of Fluid Mechanics*, accepted. doi:10.1017/jfm.2019.906.

[22] Schwamborn, D., Gerhold, T., and Heinrich, R., "The DLR TAU-Code: Recent Applications in Research and Industry," *European Conference on Computational Fluid Dynamics, ECCOMAS CFD 2006*, TU Delft, The Netherlands, 2006.

[23] Allmaras, S. R., Johnson, F. T., and Spalart, P. R., "Modifications and Clarifications for the Implementation of the Spalart-Allmaras Turbulence Model," *Seventh International Conference on Computational Fluid Dynamics*, ICCFD7–1902, Big Island, Hawaii, 2012.

[24] Sorensen, D., "Implicit Application of Polynomial Filters in a k-Step Arnoldi Method," *SIAM Journal on Matrix Analysis and Applications*, Vol. 13, No. 2, 1992, pp. 357–385.

[25] Maschhoff, K., and Sorensen, D., "P_ ARPACK: An Efficient Portable Large Scale Eigenvalue Package for Distributed Memory Parallel Architectures," *Lecture Notes in Computer Science*, Vol. 1184, 1996, pp. 478–476.

[26] Lehoucq, R., Sorensen, D., and Yang, C., *ARPACK Users' Guide*, SIAM, 1998.

[27] Xu, S., Timme, S., and Badcock, K. J., "Enabling off-design linearised aerodynamics analysis using Krylov subspace recycling technique," *Computers and Fluids*, Vol. 140, 2016, pp. 385–396.

[28] Åkervik, E., Brandt, L., Henningson, D. S., Hœpffner, J., Marxen, O., and Schlatter, P., "Steady Solutions of the Navier-Stokes Equations by Selective Frequency Damping," *Physics of Fluids*, Vol. 18, 2006, p. 068102.

[29] Plante, F., Dandois, J., and Laurendeau, E., "Similitude Between 3D Cellular Patterns in Transonic Buffet and Subsonic Stall," *AIAA Scitech 2019 Forum*, AIAA Paper 2019–0300, San Diego, California, 2019. doi:10.2514/6.2019-0300.

[30] Spalart, P., *Trends in turbulence treatments*, 2000. doi:10.2514/6.2000-2306.